Experimental Characterization of a Theoretically Designed Candidate p-Type Transparent Conducting Oxide: Li-Doped Cr_2MnO_4

Arpun R. Nagaraja,[†] Kevin H. Stone,[‡] Michael F. Toney,[‡] Haowei Peng,[§] Stephan Lany,[§] and Thomas O. Mason*,[†]

[†]Department of Materials Science and Engineering, Northwestern University, Evanston, Illinois 60208, United States
[‡]SLAC National Accelerator Laboratory, Menlo Park, California 94025, United States
[§]National Renewable Energy Laboratory, Golden, Colorado 80401, United States

S *Supporting Information*

ABSTRACT: The development of a p-type transparent conducting oxide (p-TCO) requires the deliberate design of a wide band gap and high hole conductivity. Using high-throughput theoretical screening, Cr_2MnO_4 was earlier predicted to be a p-TCO when doped with lithium. This constitutes a new class of p-TCO, one based on a tetrahedrally coordinated d^5 cation. In this study, we examine and experimentally validate a few central properties of this system. Combined neutron diffraction and anomalous X-ray diffraction experiments give site occupancy that supports the theoretical prediction that lithium occupies the tetrahedral (Mn) site. The lattice parameter of the spinel decreases with lithium content to a solubility limit of $[Li]/([Li] + [Mn]) \sim 9.5\%$. Diffuse reflectance spectroscopy measurements show that at higher doping levels the transparency is diminished, which is attributed to both the presence of octahedral Mn and the increased hole content. Room-temperature electrical measurements of doped samples reveal an increase in conductivity of several orders of magnitude as compared to that of undoped samples, and high-temperature measurements show that Cr_2MnO_4 is a band conductor, as predicted by theory. The overall agreement between theory and experiment illustrates the advantages of a theory-driven approach to materials design.
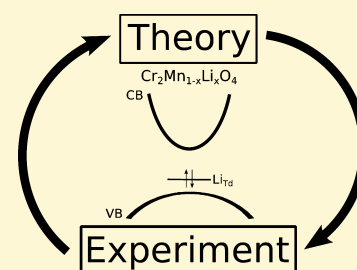
1. INTRODUCTION

A_2BO_4[1] transition metal oxides have been studied for a number of important technological applications such as colossal magnetoresistance,[2] electrodes for lithium batteries[3] and fuel cells,[4] and spintronics.[5] Recently, they have been proposed as p-type transparent conductors (p-TCOs).[6−11] The development of a high-conductivity p-TCO is a crucial step toward realizing devices like transparent flat panel displays and more efficient photovoltaics. Traditional p-TCOs like $CuAlO_2$[12,13] have a d^{10} (closed shell) electronic configuration in which the d levels are fully occupied and comprise the valence band. It was previously thought that only d^{10} compounds could be suitable p-TCOs, because a closed shell tends to promote hole delocalization at the valence band edge and because internal d−d transitions would not obscure the absorption edge. However, d^6 compounds such as the spinel Rh_2ZnO_4 have also been considered for p-TCO applications.[6,14]

A previous theoretical investigation of high-spin d^5 compounds[15] sought to design from first principles a material that would have suitable p-TCO properties. That study details a selection process in which the d^5 spinel Cr_2MnO_4 was chosen from a list of 13 candidate compounds on the basis of several design principles: (i) the ability to introduce a sufficient number of shallow acceptor states leading to free holes (enabled by substitutional Li that is predicted to have a high solubility), (ii) the absence of compensation via spontaneously generated donors (occurring when the donors are electrically inactive), (iii) the thermodynamic stability of the parent compound in a readily attainable chemical potential range, (iv) a sufficiently large band gap assuring transparency (because of the high-spin d^5 configuration that rendered the d−d transitions forbidden), and (v) good mobility allowed by a reasonably low hole effective mass and the lack of a bound polaron, both permitted by the tetrahedral coordination of the Mn ion.

With regard to conditions (i) and (ii), we note that Cr_2MnO_4 does not have any intrinsic carrier-producing defects or any intrinsic hole killers. In many spinel oxides, the most likely defects are antisite defects (A_{Td} and B_{Oh}, which indicate A cations on a tetrahedral site and B cations on an octahedral site, respectively).[10] Oxygen interstitial defects are generally considered to be energetically unfavorable because of the close-packed oxygen sublattice,[16,17] and oxygen vacancies have also been calculated to be unfavorable.[10] Because manganese readily oxidizes to Mn^{3+}, the Mn_{Oh} acceptor is neutral and does not produce any carriers. In turn, the Cr_{Td} donor has a high formation energy according to theory and confirmed by experimental site occupancy measurements on thin film samples.[10,18] Thus, Cr_2MnO_4 prefers to remain a normal spinel in which all the A cations occupy the octahedral sites and all the

B cations occupy the tetrahedral sites. Additionally, the number of carrier-producing antisite defects is negligible. Because Cr_2MnO_4 lacks intrinsic carrier-producing defects, it must be acceptor-doped to produce holes. In our previous work,[15] we predicted that lithium would be the most effective dopant, and preliminary experiments confirmed that lithium increased the conductivity of Cr_2MnO_4 by several orders of magnitude. In this study, we present a detailed experimental characterization of Li-doped Cr_2MnO_4, including site occupancy measurements, determination of the solubility limit of the dopant, optical behavior, and room- and high-temperature electrical transport studies.

2. EXPERIMENTAL METHODS

2.1. Synthesis. Bulk samples of $Cr_2Mn_{1-x}Li_xO_4$ were synthesized via solid-state reaction, with target compositions ranging from $x = 0$ to $x = 0.15$. Starting powders of chromium(III) oxide (99.97%), manganese(IV) oxide (99.997%), and lithium carbonate (99.999%) (Alfa Aesar, Ward Hill, MA) were dried overnight at 125 °C. The powders were weighed on a Mettler balance (Mettler-Toledo, Inc., Columbus, OH) with an accuracy of 0.1 mg and thoroughly ground in an agate mortar and pestle with acetone. Powders were pressed uniaxially to a pressure of approximately 120 MPa to form pellets 12.5 mm in diameter. The pellets were then surrounded by loose powder of the same composition and placed inside three nested alumina crucibles. Samples were fired at 1200 °C for 12 h and quenched to room temperature in air. Their masses and dimensions were measured and their densities calculated, ranging from 46 to 58% of the theoretical density. The theoretical density was computed from unit cell parameters obtained from fitting X-ray diffraction data as described below. Additionally, scanning electron micrographs indicated grain sizes of approximately 1 μm for the spinel phase.

2.2. Structural Characterization. X-ray diffraction on a Scintag diffractometer with a liquid nitrogen-cooled solid-state detector was used to confirm complete reaction of the starting powders. All samples contained a small amount of secondary Cr_2O_3 phase, the origin of which is discussed further below. Five of the eight samples were sent to Galbraith Laboratories for chemical analysis to measure their lithium contents, and their target values were compared with their actual values. A linear relationship between these two quantities was found, so a linear interpolation was used to estimate the lithium content of samples that were not measured. It was found that the average Li_2CO_3 mass difference between the loading composition and final composition for all doped samples was approximately −0.7 mg. This corresponds to an average difference of −0.4% between the target and actual x values. In Figures 1 and 3, the estimated lithium content is presented. In the text, target compositions are noted where applicable.

For Rietveld analysis of doped samples, high-resolution synchrotron powder X-ray diffraction data were collected with an average wavelength of 0.469659 Å at the Advanced Photon Source (APS, Argonne National Laboratory, Lemont, IL) using the Rapid Access program. The lattice parameter of the spinel phase and the relative amounts of each phase present were quantitatively determined using the General Structure Analysis System (GSAS)[19] with the EXPGUI interface.[20] χ^2 values ranged between 2 and 4.5, which indicates good agreement between the experimental and fitted patterns.[21]

For target compositions of $x < 10\%$, the only phases detected in the samples were spinel and Cr_2O_3. For target compositions of $x \geq 10\%$, an additional phase, $LiCrO_2$, was detected. Samples also contained a small amount of silicon standard, which was mechanically mixed into them prior to structural characterization. All phase fractions reported here are adjusted for the presence of the silicon.

2.3. Site Occupancy Measurement. To determine the site occupancies of the undoped and $x = 7.5\%$ samples, simultaneous Rietveld refinement of constant-wavelength neutron and anomalous synchrotron X-ray powder diffraction data was performed. Neutron powder diffraction data were collected using the BT-1 32 detector neutron powder diffractometer at the National Institute of Standards

and Technology Center for Neutron Research (NCNR). Approximately 2 g of material was loaded into a vanadium cell in a dry helium environment. Neutrons with a wavelength of 1.540 Å were selected using a Cu(311) monochromator with an in-pile 60′ collimator. Data were collected over a 2θ range of 3−168° in 0.05° steps. Synchrotron X-ray data were collected at beamline 2-1 at the Stanford Synchrotron Radiation Lightsource (SSRL) using a Vortex silicon drift detector behind 1 mrad Soller slits. Data were collected at two different X-ray energies selected by a Si(111) double-bounce monochromator. X-ray energies of 9650 and 6545 eV were chosen to give one data set just below the Mn K-edge and one well above resonance.

These three data sets for each sample were co-refined using the Rietveld software TOPAS-Academic.[22] The model included two crystalline phases for the X-ray data (Cr_2O_3 and Cr_2MnO_4) with the addition of vanadium for the neutron data. All parameters were the same with the exception of thermal parameters, which were allowed to vary independently for the neutron data.

Refinement was performed by constraining the Oh/Td site ratio to 2 to account for the presence of Cr_2O_3. This means that although the ratio is constant, the sum of octahedral species may not be 2 and the sum of tetrahedral species may not be 1. The cation/oxygen ratio was also constrained to be 3/4, and $[Li_{Oh}]$ and $[Cr_{Td}]$ were constrained to be 0, because theoretical calculations indicated that oxygen vacancies, Li_{Oh}, and Cr_{Td} are unlikely to occur in this system.[15] Site occupancies were refined with two free parameters, x and y, according to

$$[Cr_{2-3y}Mn_y]_{Oh}(Mn_{1-x-y}Li_x)_{Td}O_{4(1-y)}$$

where subscripts Oh and Td denote the octahedral and tetrahedral sites, respectively. X-ray thermal parameters were constrained to be equal for all atoms on a given site, and a similar constraint was imposed for the neutron data. The phase fraction of Cr_2O_3 was allowed to be freely refined.

2.4. Optical Characterization. The optical band gaps of bulk samples ($x = 0−7.5\%$) were measured using diffuse reflectance spectroscopy with a Lambda 1050 UV−vis spectrophotometer (PerkinElmer, Inc.) with the integrating sphere attachment; 100% reflectance and 0% reflectance baselines were taken prior to sample measurement. Kubelka−Munk analysis[23] was performed on the data to determine the positions of the absorption edges. Although the samples do contain a secondary Cr_2O_3 phase, the maximal amount is <4 wt %, so it is not expected to interfere with the measurement.

2.5. Electrical Characterization. The room-temperature four-point dc electrical conductivity of bulk samples was measured using a method described in detail by Hong et al.[24] Rectangular bar specimens were cut from pellets using a diamond saw and then wrapped with gold wire at positions approximately one-third of the length from each end (voltage leads). The samples were then sandwiched between gold foils (current leads). Electrodes, which doubled as thermocouples, were attached to the gold wire loops and foils. For high-temperature measurements, samples were placed in a flowing gas tube furnace just outside the hot zone to induce a temperature gradient. A computer-controlled current source and multimeter were employed to measure the dc resistances and Seebeck coefficients of the samples at various temperatures. All measurements were performed in dry air. All reported conductivities were corrected for porosity using the Bruggeman symmetric model as described by McLachlan et al.[25] The secondary Cr_2O_3 and $LiCrO_2$ phases (when present) were treated as insulating pores, because bulk samples of each were fabricated and measured to be electrically insulating.

High-temperature two-point AC impedance spectroscopy (ACIS) measurements were also performed on a sample with an $x = 5\%$ target composition. The impedance was measured between frequencies of 13 MHz and 10 Hz using an oscillating voltage of 500 mV. The ends of the bar sample were sputtered with 150 nm of gold and then painted with gold conducting paste. The paste was cured in a furnace at 150 °C for approximately 2 h, and the sample was allowed to cool to room temperature before measurements were performed.

ACIS spectra are typically fit using an equivalent circuit model. Each arc in the Nyquist plot $[-Im(Z) \text{ vs } Re(Z)]$ is modeled with a resistor

(R) and constant phase element (Q) in parallel. The constant phase element, which represents an imperfect capacitor associated with inhomogeneities, for example, a range of grain sizes and/or grain boundary barrier thicknesses, which corresponds to depression of the impedance arc below the real axis, is related to the capacitance (C) by

$$C = (QR^{1-n})^{1/n}$$

A constant phase element that acts as an ideal capacitor shows no arc depression and would have $n = 1$. If there are multiple arcs in a given spectrum, the system is modeled by multiple RQ circuits in series.

3. RESULTS AND DISCUSSION

3.1. Site Occupancy. The site occupancies of undoped Cr_2MnO_4 and doped $Cr_2Mn_{1-x}Li_xO_4$ with $x = 0.075$ were measured. The undoped sample was a normal spinel, although the presence of the secondary Cr_2O_3 phase (~1 wt %) indicates that there is likely some Mn_{Oh} that is below the detection limit of the technique. The doped sample contained approximately 2 wt % Cr_2O_3 and had a site occupancy of $[Cr_{1.81}Mn_{0.06}]_{Oh}(Mn_{0.84}Li_{0.10})_{Td}$. The error in the site occupancies is approximately ±0.02, as indicated by the deviation of the measured Li_{Td} value as compared to the target value of 0.075, as well as the change in R_{wp} upon manual adjustment of site occupancy values.

This site occupancy measurement is consistent with the theoretical prediction that Li occupies the tetrahedral site in the spinel structure. Although Li_{Oh} species were constrained to be zero during refinement, relaxing this constraint brings the Li_{Oh} occupancy to a value of only 0.01, which is within the error of the technique. Additionally, because roughly 3.3% of the octahedral sites are occupied by Mn, it appears that the presence of lithium causes some Mn atoms to occupy the octahedral site. The co-refinement of the diffraction data strongly supports the preference for Li to dope the tetrahedral site, as predicted by theory.

3.2. Solubility Limit of Li in Cr_2MnO_4. Vegard's law was used to estimate the solubility limit of lithium in the Cr_2MnO_4 spinel phase (Figure 1). The lattice parameter of the spinel
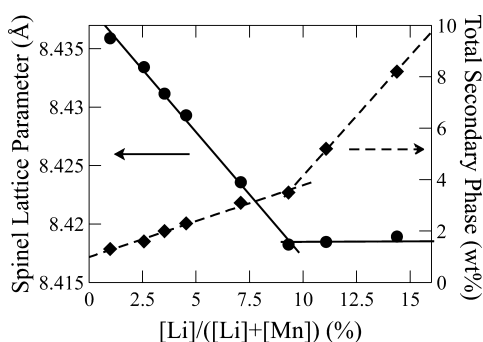

Figure 1. Lattice parameter of spinel phase and total secondary phase content as a function of the estimated lithium concentration.

decreases steadily with lithium content, as expected for substitutional lithium. At values of $x > 9.5\%$, the lattice parameter becomes constant. A similar trend is seen in the total secondary phase content as a function of lithium content. Below the solubility limit, the amount of Cr_2O_3 in the sample linearly increases with an increasing lithium content. Beyond the solubility limit, $LiCrO_2$ begins to form, and the total secondary phase content increases.

Samples with no lithium ($x = 0$) also contained a small amount of Cr_2O_3 (<1 wt %). The solid solution in the Mn−Cr−O system can be represented by $Cr_{2-\alpha}Mn_{1+\alpha}O_4$. Some previous experimental studies[26,27] have determined that for the synthesis conditions used in this work ($T = 1200$ °C, and $p_{O_2} = 0.2$ atm), the phase boundary between the spinel and Cr_2O_3 is at a value of $\alpha = 0$. However, other experimental[28] and theoretical[29] studies provided evidence that the phase boundary is actually at a value of $\alpha > 0$, meaning that at a target composition of $\alpha = 0$, the system would actually be in a two-phase region of spinel and Cr_2O_3, which is consistent with the results seen in this work.

The lattice parameter measurements indicate that the maximum solubility of lithium in the spinel is at $x \sim 9.5\%$. Although the thermodynamically predicted solubility limit is $x \sim 2.4\%$, this discrepancy is within error of the theoretical prediction, considering that thermal effects such as vibrational entropy and the temperature dependence of the band structure were not taken into account when calculating the enthalpy of formation of the Li_{Td} species.[15] It is also possible that there are kinetic effects that favor the incorporation of Li into Cr_2MnO_4 over the precipitation of the $LiCrO_2$ secondary phase. In particular, the nucleation of $LiCrO_2$ crystals is associated with surface/interface energies that could "delay" the occurrence of $LiCrO_2$ to higher Li compositions beyond the actual thermodynamic solubility limit. The precise mechanism behind the behavior of the secondary Cr_2O_3 content is also unknown, but a likely explanation is that during synthesis, the Li_2CO_3 reactant may create relatively oxidizing conditions that drive the spinel composition toward the Mn-rich end of the solid solution. The increased amount of Mn_{Oh}^{3+} in the spinel, confirmed by the site occupancy measurements, accounts for the increased amount of secondary Cr_2O_3 detected. The low Mn_{Oh} concentration present in these samples does not have a measurable effect on the electrical properties.

3.3. Optical Properties. Figure 2 shows Kubelka−Munk absorption spectra of undoped Cr_2MnO_4, undoped $Cr_{1.8}Mn_{1.2}O_4$, and two doped samples ($x = 1$ and 7.5%). The undoped Cr_2MnO_4 has an absorption edge at approximately 3.2 eV, in excellent agreement with the band gap of 3.34 eV
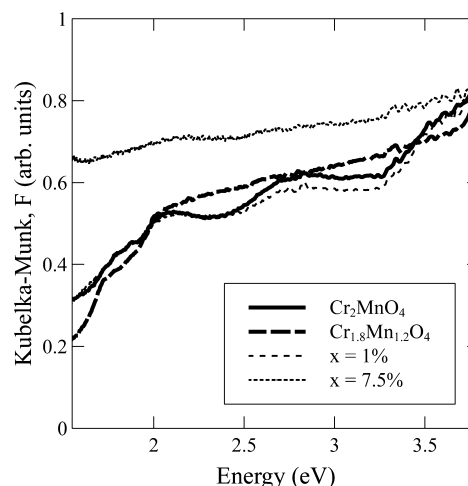

Figure 2. Kubelka−Munk function of diffuse reflectance data on undoped Cr_2MnO_4, $Cr_{1.8}Mn_{1.2}O_4$ (thicker lines), and two Li-doped Cr_2MnO_4 samples (thinner lines). Doped samples exhibit diminished optical transparency relative to that of undoped samples.

predicted by theory. There is an additional absorption edge at 2.3 eV, which is attributed to internal d−d transitions in chromium.[30] Although the bulk pellet is a light green color, transmission measurements on thin film samples showed that the d−d transitions do not significantly contribute to optical absorption.[15]

With small amounts of lithium (x = 1%), the optical transparency of the spinel is relatively unchanged. At higher lithium doping levels, the absorption increases noticeably, with the color of samples changing from green to black. This behavior can be partially explained by the presence of Mn_{Oh}, because this species has an unoccupied d level that causes absorption of visible light.[15] However, this effect cannot be explained by Mn_{Oh} defects alone. Optical measurements on a sample of undoped $Cr_{1.8}Mn_{1.2}O_4$, in which $[Mn_{Oh}]/([Mn_{Oh}] + [Cr_{Oh}]) = 10\%$, show that it does have reduced transparency, but this loss is not as significant as in the x = 7.5% sample, in which $[Mn_{Oh}]/([Mn_{Oh}] + [Cr_{Oh}])$ was measured to be only 3.3%.

Instead, this behavior is attributed to the increase in carrier content caused by Li doping. Incident photons of subgap energies are absorbed because they cause excitation of electrons from lower-lying states in the valence band to the empty states near the valence band maximum. This apparent trade-off between conductivity and transparency is well-known in the p-TCO literature[13,31−34] and can be overcome only by finding a material with a dispersed valence band such that the lowest-energy transition within the band is in the ultraviolet region.

3.4. Electrical Properties and Polaron. Figure 3 shows the room-temperature electrical conductivity of rectangular bar
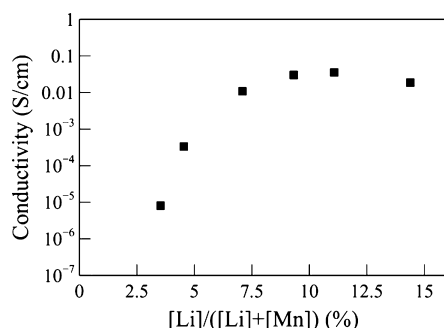

Figure 3. Room-temperature four-point dc conductivity of bar-shaped polycrystalline samples as a function of the estimated lithium content.

samples as a function of the estimated lithium content. The conductivity increases exponentially with lithium content until the solubility limit, beyond which the variation in conductivity is small. The maximum conductivity measured at room temperature was 3.5×10^{-2} S/cm, which is similar to that of other traditional p-TCOs like the d^{10} compound $CuAlO_2$.[12,13] Room-temperature high-field Hall effect measurements were also attempted, but the results were inconclusive and suggested a mobility of <1 cm^2 V^{-1} s^{-1}. This value is similar to those of other reported p-TCOs. On the basis of this estimate, the hole content of the highest-conductivity sample is most likely >10^{17} cm^{-3}.

In our previous work,[15] Cr_2MnO_4 was predicted to be a band conductor by first-principles calculations, which contradicts a previous report of small polaron hopping in the Mn−Cr−O system by Lu et al.[35] Below, we summarize an analysis that combines high-temperature measurements of conductivity and

thermopower, as well as theoretical calculations of the effective density of states to infer the existence of an activated mobility that, if present, is usually indicative of small polaron hopping. This analysis is more rigorously presented by Nagaraja et al.[36]

The conductivity (σ) and reduced thermopower (Q_{red}) of a p-type material can be expressed with the following equations:

$$\sigma = pe\mu \tag{1}$$

where p is the hole concentration, e is the fundamental electron charge, and μ is the mobility and

$$Q_{red} = -\frac{Q}{k/e} = \ln p - \ln N_V - A \tag{2}$$

where k is Boltzmann's constant, N_V is the effective density of states, and A is a transport constant that is typically between 2 and 4 for band conductors and 0 for small polaron conductors. Combining these equations eliminates the dependence on the carrier content to yield

$$\ln \sigma - Q_{red} - \ln N_V = \ln \mu + \ln e + A \tag{3}$$

The last two terms in eq 3 are constants. Thus, the measurements of σ and Q_{red} at various temperatures, combined with N_V, yield the temperature dependence of the mobility. In this case, N_V was calculated using density functional theory, but the classical $T^{3/2}$ dependence can be applied in the absence of theoretical calculations.

Figure 4 shows the conductivity, thermopower, and quantity in eq 3 of two doped samples with target compositions of x = 5 and 10% as a function of inverse temperature. At higher temperatures, above approximately 450 °C (to the left of the gray box in the figure), the mobility is invariant with temperature, which is indicative of band conduction. At low temperatures, even with the correction for the effective density of states, the mobility appears to be activated. In the past, this behavior would have been considered evidence of small polaron conduction,[37−41] but first-principles calculations have suggested that a band conduction mechanism is energetically favorable.

Instead, the apparent temperature dependence of the mobility can be attributed to grain boundary scattering. This effect was first proposed by Seto for polycrystalline silicon films in which disorder at grain boundaries caused carrier trapping, resulting in a potential barrier.[42] Since then, potential barriers in polycrystalline ceramics have been studied extensively using a Schottky barrier model. For example, in nanocrystalline ceria[43] and microcrystalline Gd-doped ceria (GDC),[44] well-known oxygen ion conductors, ac impedance spectroscopy (ACIS) was used to show that space charges from potential barriers had a significant effect on carrier transport and that the size of the potential barrier depended on the amount of dopant. In Y-doped zirconia, the Schottky barrier model accurately reproduced experimental features seen in impedance spectra.[45] Potential barriers have also been observed in protonic conductors,[46] mixed ionic−electronic conductors,[47] and electronic conductors.[48]

To investigate the effect of grain boundaries on electrical conductivity, ACIS was performed on the sample with a target composition of x = 5% after high-temperature electrical measurements. The room-temperature data are shown in a Nyquist plot in Figure 5 (circles). Although the high-frequency contribution is incomplete, there is clear evidence of dual-arc behavior, so the data were fit using a resistor and RQ element in series as shown in the figure. At 25 °C, n = 0.775, and at 44 °C, n = 0.848.
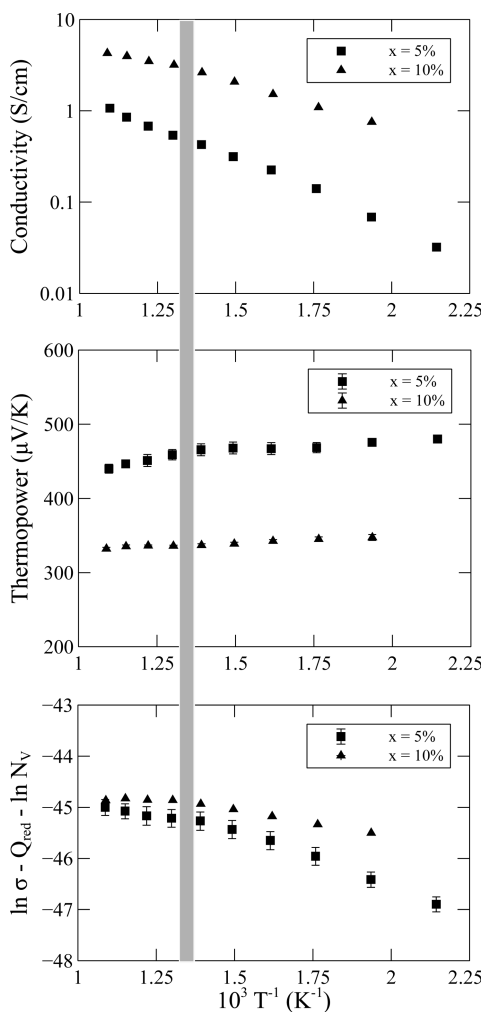
Figure 4. High-temperature conductivity (top), thermopower (middle), and activated mobility analysis (bottom) of two doped samples. The shaded area represents the temperature range over which a change in slope for the electrical properties occurs.

Figure 5. Nyquist plots of ACIS data from a $Cr_2Mn_{1-x}Li_xO_4$ sample with a target composition of $x = 5\%$. At room temperature, the measured dc four-point resistance matches the sum of the grain core (R_{GC}) and grain boundary (R_{GB}) resistances. The left inset shows an equivalent circuit model used to fit ACIS data. The right inset shows that as the temperature increases, the grain boundary's contribution to the overall resistance decreases.

Figure 6. Arrhenius plot of the grain boundary resistance. The nonlinear behavior indicates that the potential barrier also exhibits a temperature dependence.

For $Cr_2Mn_{1-x}Li_xO_4$ samples with a bar geometry, the expected capacitance for the grain core contribution is ~0.01 pF using a dielectric constant (ε) of 4, which was measured for bulk Cr_2MnO_4 samples.[49] On the basis of this value, the capacitance of the grain boundary contribution would be ~10 pF. From the values of R, Q, and n obtained from the fit, the capacitance of the low-frequency (right-most) arc is 10.2 pF, which agrees well with the expected grain boundary contribution. Thus, this arc is attributed to the grain boundary resistance (R_{GB}), which is caused by a potential barrier. The high-frequency arc, then, represents the grain core resistance (R_{GC}). The dc four-point resistance is in good agreement with the sum $R_{GC} + R_{GB}$, as expected.

At elevated temperatures, the high-frequency arc shifts beyond the frequency range of the impedance analyzer, but the high-frequency intercept of the GB arc on the real axis can be taken as the GC resistance. Figure 6 shows an Arrhenius plot of the grain boundary resistance. As the temperature increases, R_{GB} decreases as expected for carrier transport in the presence of a potential barrier. The trend is nonlinear, which indicates that the size of the potential barrier is also a function of temperature. This is certainly possible if the defects responsible
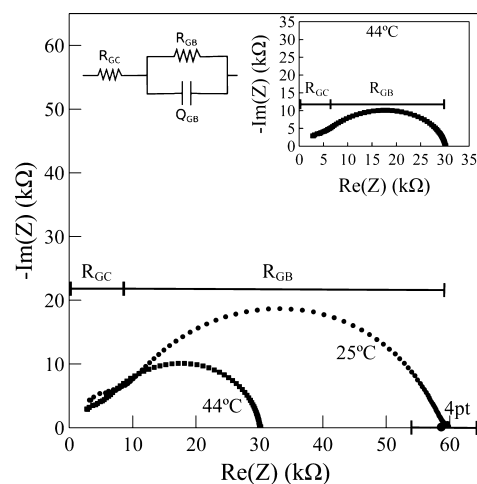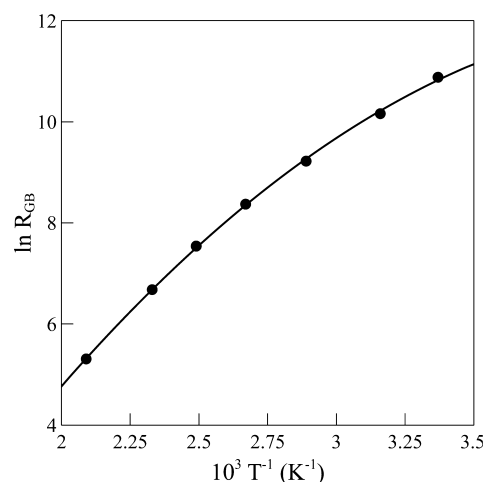
for the potential barrier also change with temperature, as observed in GDC.[44]

Because the exact functional form of the temperature dependence of the barrier height is unknown, it can be modeled using a Taylor expansion, which accurately reproduced the temperature dependence in GDC: $\Phi(T) = \Phi_0 + (1/T)\{(\partial\Phi)/[\partial(1/T)]\}$. Using a Taylor expansion, the Arrhenius behavior of R_{GB} can be fit with a second-order polynomial. Extrapolating this fit to higher temperatures, we find that at 450 °C, the temperature at which the slope transition occurs, the grain boundary resistance decreases to 2 Ω, which is <5% of the overall sample resistance. We therefore attribute the change in the slope to the reduced effect of the grain boundary potential barriers on itinerant band conduction of free holes.

This suggests that even higher values of conductivity should be possible for Li-doped Cr_2MnO_4 in the absence of grain boundaries, e.g., in single crystals or epitaxial/highly oriented thin films.

4. CONCLUSION

The inverse design approach to materials discovery was applied to developing a novel p-type transparent conducting oxide, and the d^5 spinel Cr_2MnO_4 was predicted to be a good candidate after extrinsic doping. The structural, optical, and electrical properties of various compositions of bulk, polycrystalline Li-doped Cr_2MnO_4 were characterized. It was found that lithium is an effective dopant, increasing the p-type electrical conductivity of the spinel by several orders of magnitude at room temperature. High-temperature transport measurements confirm the prediction that Cr_2MnO_4 is a band conductor whose electrical properties may be further improved by the elimination of grain boundaries, for example, in single crystals and epitaxial/highly oriented thin films. However, Li doping of Cr_2MnO_4 reduces the optical transparency, which is attributed to the presence of Mn_{Oh} species and the increased hole content.

■ ASSOCIATED CONTENT

Ⓢ Supporting Information

Powder neutron diffraction and anomalous X-ray diffraction spectra of a doped bulk sample. This material is available free of charge via the Internet at http://pubs.acs.org.

■ AUTHOR INFORMATION

Corresponding Author

*E-mail: t-mason@northwestern.edu.

■ REFERENCES

(1) Another widely used way of writing the spinel chemical formula is AB_2O_4. We, however, write A_2BO_4, which is common for spinels with formal cation valencies of $Z_A = 2$ and $Z_B = 4$ such as Mg_2TiO_4. The main reason for our choice is because the work presented here is part of a larger project that treats all A_2BX_4 compounds (not only spinels) in different structure types, including olivine Fe_2SiO_4, β-K_2SO_4, or La_2CuO_4, for which A_2BX_4 is the generally used notation.

(2) Philip, J.; Kutty, T. R. N. *Mater. Lett.* **1999**, *39*, 311−317.

(3) Thackeray, M. M. *Prog. Solid State Chem.* **1997**, *25*, 1−71.

(4) Liu, H. Y.; Zhu, X. F.; Cheng, M. J.; Cong, Y.; Yang, W. S. *Int. J. Hydrogen Energy* **2013**, *38*, 1052−1057.

(5) Yamasaki, Y.; Miyasaka, S.; Kaneko, Y.; He, J. P.; Arima, T.; Tokura, Y. *Phys. Rev. Lett.* **2006**, *96*, 207204-1.

(6) Dekkers, M.; Rijnders, G.; Blank, D. H. A. *Appl. Phys. Lett.* **2007**, *90*, 021903-1.

(7) Exarhos, G. J.; Zhou, X. D. *Thin Solid Films* **2007**, *515*, 7025−7052.

(8) Windisch, C. F.; Exarhos, G. J.; Ferris, K. F.; Engelhard, M. H.; Stewart, D. C. *Thin Solid Films* **2001**, *398*, 45−52.

(9) Windisch, C. F.; Ferris, K. F.; Exarhos, G. J.; Sharma, S. K. *Thin Solid Films* **2002**, *420*, 89−99.

(10) Paudel, T. R.; Zakutayev, A.; d'Avezac, M.; Lany, S.; Zunger, A. *Adv. Funct. Mater.* **2011**, *21*, 4493−4501.

(11) Perkins, J. D.; Paudel, T. R.; Zakutayev, A.; Ndione, P. F.; Parilla, P. A.; Young, D. L.; Lany, S.; Ginley, D. S.; Zunger, A.; Perry, N. H.; Tang, Y.; Grayson, M.; Mason, T. O.; Bettinger, J. S.; Shi, Y.; Toney, M. F. *Phys. Rev. B* **2011**, *84*, 205207-1.

(12) Kawazoe, H.; Yasukawa, M.; Hyodo, H.; Kurita, M.; Yanagi, H.; Hosono, H. *Nature* **1997**, *389*, 939−942.

(13) Tate, J.; Ju, H. L.; Moon, J. C.; Zakutayev, A.; Richard, A. P.; Russell, J.; McIntyre, D. H. *Phys. Rev. B* **2009**, *80*, 165206-1.

(14) Scanlon, D. O.; Watson, G. W. *Phys. Chem. Chem. Phys.* **2011**, *13*, 9667−9675.

(15) Peng, H.; Zakutayev, A.; Lany, S.; Paudel, T. R.; d'Avezac, M.; Ndione, P.; Perkins, J. D.; Ginley, D. S.; Nagaraja, A. R.; Perry, N. H.; Mason, T. O.; Zunger, A. *Adv. Funct. Mater.* **2013**, *23*, 5267−5276.

(16) Ting, C. J.; Lu, H. Y. *J. Am. Ceram. Soc.* **1999**, *82*, 841−848.

(17) White, G. S.; Jones, R. V.; Crawford, J. H. *J. Appl. Phys.* **1982**, *53*, 265−270.

(18) Shi, Y.; Ndione, P. F.; Lim, L. Y.; Sokaras, D.; Weng, T.-C.; Nagaraja, A. R.; Karydas, A. G.; Perkins, J. D.; Mason, T. O.; Ginley, D. S.; Zunger, A.; Toney, M. F. *Chem. Mater.* **2014**, *26*, 1867−1873.

(19) Larson, A. C.; Von Dreele, R. B. Los Alamos National Laboratory Report LAUR 86-748; Los Alamos National Laboratory: Los Alamos, NM, 2000.

(20) Toby, B. H. *J. Appl. Crystallogr.* **2001**, *34*, 210−213.

(21) Toby, B. H. *Powder Diffr.* **2006**, *21*, 67−70.

(22) Coelho, A. A. *TOPAS-Academic*, version 3; 2007.

(23) Kubelka, P.; Munk, F. *Z. Tech. Phys.* **1931**, *12*, 593−601.

(24) Hong, B. S.; Ford, S. J.; Mason, T. O. *Electrical Properties of Oxide Materials*; Scientific.Net: Pfaffikon, Switzerland, 1997; Vol. *125*, pp 163−185.

(25) Mclachlan, D. S.; Blaszkiewicz, M.; Newnham, R. E. *J. Am. Ceram. Soc.* **1990**, *73*, 2187−2203.

(26) Pollert, E.; Nevriva, M.; Novak, J. *Mater. Res. Bull.* **1980**, *15*, 1453−1456.

(27) Golikov, Y. V.; Bamburov, D. V.; Barkhatov, V. P.; Balakirev, V. F. *J. Phys. Chem. Solids* **1985**, *46*, 1357−1360.

(28) Speidel, D. H.; Muan, A. *J. Am. Ceram. Soc.* **1963**, *46*, 577−578.

(29) Jung, I. H. *Solid State Ionics* **2006**, *177*, 765−777.

(30) Cheng, C. S.; Gomi, H.; Sakata, H. *Phys. Status Solidi A* **1996**, *155*, 417−425.

(31) Dutta, T.; Gupta, P.; Gupta, A.; Narayan, J. *J. Appl. Phys.* **2010**, *108*, 083715-1.

(32) Nagarajan, R.; Draeseke, A. D.; Sleight, A. W.; Tate, J. *J. Appl. Phys.* **2001**, *89*, 8022−8025.

(33) Sadik, P. W.; Ivill, M.; Craciun, V.; Norton, D. P. *Thin Solid Films* **2009**, *517*, 3211−3215.

(34) Tate, J.; Jayaraj, M. K.; Draeseke, A. D.; Ulbrich, T.; Sleight, A. W.; Vanaja, K. A.; Nagarajan, R.; Wager, J. F.; Hoffman, R. L. *Thin Solid Films* **2002**, *411*, 119−124.

(35) Lu, Z. G.; Zhu, J. H.; Payzant, E. A.; Paranthaman, M. P. *J. Am. Ceram. Soc.* **2005**, *88*, 1050−1053.

(36) Nagaraja, A. R.; Perry, N. H.; Mason, T. O.; Tang, Y.; Grayson, M.; Paudel, T. R.; Lany, S.; Zunger, A. *J. Am. Ceram. Soc.* **2012**, *95*, 269−274.

(37) Chen, H. C.; Gartstein, E.; Mason, T. O. *J. Phys. Chem. Solids* **1982**, *43*, 991−995.

(38) Ingram, B. J.; Mason, T. O.; Asahi, R.; Park, K. T.; Freeman, A. J. *Phys. Rev. B* **2001**, *64*, 155114-1.

(39) Karim, D. P.; Aldred, A. T. *Phys. Rev. B* **1979**, *20*, 2255−2263.

(40) Tuller, H. L.; Nowick, A. S. *J. Phys. Chem. Solids* **1977**, *38*, 859−867.

(41) Crevecoeur, C.; De Wit, H. J. *J. Phys. Chem. Solids* **1970**, *31*, 783−791.

(42) Seto, J. Y. W. *J. Appl. Phys.* **1975**, *46*, 5247−5254.

(43) Kim, S.; Maier, J. *J. Electrochem. Soc.* **2002**, *149*, J73−J83.

(44) Avila-Paredes, H. J.; Choi, K.; Chen, C. T.; Kim, S. *J. Mater. Chem.* **2009**, *19*, 4837−4842.

(45) Guo, X.; Maier, J. *J. Electrochem. Soc.* **2001**, *148*, E121−E126.

(46) Iguchi, F.; Chen, C. T.; Yugami, H.; Kim, S. *J. Mater. Chem.* **2011**, *21*, 16517−16523.

(47) Hagenbeck, R.; Waser, R. *J. Appl. Phys.* **1998**, *83*, 2083−2092.

(48) Felix, A. A.; Orlandi, M. O.; Varela, J. A. *Solid State Commun.* **2011**, *151*, 1377−1381.

(49) Song, S. H.; Yuan, Z. X.; Xiao, P. *J. Mater. Sci. Lett.* **2003**, *22*, 755−757.